

Vanadocene *de Novo*: Spectroscopic and Computational Analysis of Bis(η^5 -cyclopentadienyl)vanadium(II)

Timothy A. Jackson,*† J. Krzystek,‡ Andrew Ozarowski,‡ Gayan B. Wijeratne,† Benjamin F. Wicker,§ Daniel J. Mindiola,§ and Joshua Telser*,⊥

†Department of Chemistry, University of Kansas, 1251 Wescoe Hall Drive, Lawrence, Kansas 66045, United States

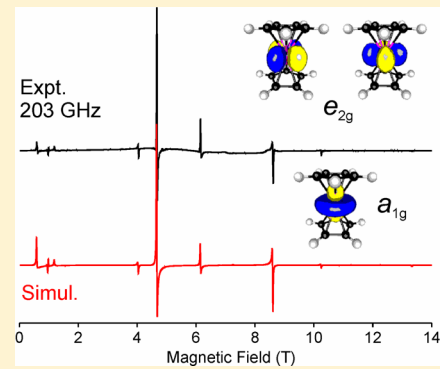
‡National High Magnetic Field Laboratory, Florida State University, Tallahassee, Florida 32310, United States

§Department of Chemistry, Indiana University, Bloomington, Indiana 47405, United States

⊥Department of Biological, Chemical and Physical Sciences, Roosevelt University, Chicago, Illinois 60605, United States

S Supporting Information

ABSTRACT: The magnetic and electronic properties of the long-known organometallic complex vanadocene (VCp_2), which has an $S = 3/2$ ground state, were investigated using conventional (X-band) electron paramagnetic resonance (EPR) and high-frequency and -field EPR (HFEPR), electronic absorption, and variable-temperature magnetic circular dichroism (VT-MCD) spectroscopies. Frozen toluene solution X-band EPR spectra were well resolved, yielding the ${}^{51}\text{V}$ hyperfine coupling constants, while HFEPR were also of outstanding quality and allowed ready determination of the rigorously axial zero-field splitting of the spin quartet ground state of VCp_2 : $D = +2.836(2) \text{ cm}^{-1}$, $g_{\perp} = 1.991(2)$, $g_{\parallel} = 2.001(2)$. Electronic absorption and VT-MCD studies on VCp_2 support earlier assignments that the absorption signals at 17 000, 19 860, and 24 580 cm^{-1} are due to ligand-field transitions from the ${}^4\text{A}_{2g}$ ground state to the ${}^4\text{E}_{1g}$, ${}^4\text{E}_{2g}$, and ${}^4\text{E}_{1g}$ excited states, using symmetry labels from the D_{5d} point group (i.e., staggered VCp_2). Contributions to the D parameter in VCp_2 and further insights into electronic structure were obtained from both density functional theory (DFT) and multireference SORCI computations using X-ray diffraction structures and DFT-energy-minimized structures of VCp_2 . Accurate D values for all models considered were obtained from DFT calculations ($D = 2.85\text{--}2.96 \text{ cm}^{-1}$), which was initially surprising, because the orbitally degenerate excited states of VCp_2 cannot be properly treated by DFT methods, as they require a multideterminant description. Therefore, D values were also computed using the SORCI (spectroscopically oriented configuration interaction) method, which provides multireference descriptions of ground and excited states. SORCI calculations gave accurate D values ($2.86\text{--}2.90 \text{ cm}^{-1}$), where the dominant (~80%) contribution to D arises from spin-orbit coupling between ligand-field states, with the largest contribution from a low-lying ${}^2\text{A}_{1g}$ state. In contrast, the D value obtained by the DFT method is achieved only fortuitously, through cancellation of errors. Furthermore, the SORCI calculations predict ligand-field excited-state energies within 1300 cm^{-1} of the experimental values, whereas the corresponding time-dependent DFT calculations fail to reproduce the proper ordering of excited states. Moreover, classical ligand-field theory was validated and expanded in the present study. Thus older theory still has a place in the analysis of paramagnetic organometallic complexes, along with the latest *ab initio* methods.



INTRODUCTION

For the past sixty years, metallocenes have occupied one of the most prominent positions in organometallic chemistry. The classical metallocene (or a sandwich-like structure) is one with bis(η^5 -cyclopentadienyl) ligands and the metal ion in the 2+ formal oxidation state, MCp_2 . For cases where the metal ion is in an odd-numbered group, paramagnetic MCp_2 complexes result.^{1,2} These include vanadocene (VCp_2 , V^{II} , 3d^3),³ manganocene (MnCp_2 , Mn^{II} , 3d^5),^{4–6} and cobaltocene (CoCp_2 , Co^{II} , 3d^7).⁷ The orbital degeneracy of the highly symmetric (staggered, D_{5d} or eclipsed, D_{5h}) MCp_2 complex means that paramagnetic species can also result for M^{II} ions with even electron count, such as for chromocene (CrCp_2 , Cr^{II} , 3d^4)⁸ and nickelocene (NiCp_2 , Ni^{II} , 3d^8).⁹ The MO diagram for

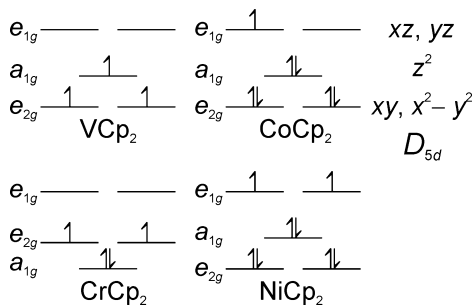
several such systems is shown qualitatively in Scheme 1. Note that the ordering of the a_{1g} (d_{z^2} orbital in D_{5d} point group symmetry) and the e_{2g} (d_{xy} , $d_{x^2-y^2}$ orbitals) can vary; yet of those shown, only for chromocene would this ordering affect the spin ground state.

Paramagnetic metallocene complexes were investigated by electron paramagnetic resonance (EPR)¹⁰ spectroscopy very early on, such as vanadocene by McConnell and co-workers in 1959¹¹ and by others soon thereafter.^{3,12} Other metallocenes, such as cobaltocene, as well as metallocenium ions, such as ferrocenium ($[\text{FeCp}_2]^+$),¹³ have been the subject of very

Received: September 18, 2012

Published: November 14, 2012

Scheme 1



detailed EPR investigations.^{5,14} EPR spectroscopy contributed data that were important in the fundamental understanding of electronic structure and bonding in paramagnetic metallocenes as well as paramagnetic organometallic complexes in general.

These early studies used state-of-the-art experimental techniques and theoretical models. However, they were limited by existing instrumentation and, even more so, restricted by computing power. Since that time, however, there have been significant advances in both experimental and theoretical methodology. These include the use of high magnetic fields and corresponding high frequencies in EPR spectroscopy, which has been applied over the past 15 years to a variety of transition metal ion complexes with $S > 1/2$ ground states.¹⁵ Other techniques such as inelastic neutron scattering (INS) have been applied to complexes of interest here, such as nickelocene,⁹ which has an $S = 1$ spin ground state. Perhaps more significant are the advances in computational chemistry, so that DFT calculations on open-shell transition metal complexes are now becoming quite routine.^{16,17} Nevertheless, DFT methods can give questionable results when applied in particular to complexes with $S > 1/2$ ground states, especially with regard to properties that require accurate treatment of excited states.^{18–21} While DFT methods were previously employed to provide detailed insights into the structural and electronic properties of MCp_2 complexes (where $M = \text{V}, \text{Cr}, \text{Mn}, \text{Fe}$, and Co), that work did not include consideration of magnetic parameters.²² In addition, orbital degeneracy in the ground and/or excited states of these metallocenes poses a problem for a DFT approach, as such states require the use of multideterminant methods. For calculating the properties of such systems, the state of the art is to use *ab initio* methods, such as CASSCF, which, however, are more computationally demanding and require judicious user input in the selection of appropriate active spaces.²³ In particular, the multireference configuration interaction method SORCI (spectroscopically oriented configuration interaction), which was designed by Neese as a robust, general method for predicting energy differences between multireference ground and excited states,²⁴ has proven quite reliable in the prediction of magnetic properties; however, because of its high computational demands, it is often limited to truncated models of actual systems.^{18,19,21}

As a part of the efforts of some of us to study low-coordination-number, reactive, early transition metal complexes,²⁵ we have been applying EPR spectroscopy, in particular HFEPR, to paramagnetic organometallic complexes of V^{II} and $\text{V}^{\text{III}}.$ ^{26,27} The realization as to how little was known about the electronic structure of such species led us to revisit a paradigm of this type of complex, namely, vanadocene, with its $S = 3/2$

ground state, using the latest experimental and computational techniques available to us.

We have found that the original work,³ both experimental and theoretical (using ligand-field theory), was remarkably successful at describing the electronic structure of VCp_2 , given the technology available at that time. Yet the application of a combination of modern experimental and theoretical methods has yielded deeper insight into this important organometallic complex and definitively described its electronic structure. In general, knowledge of electronic structure can be a powerful tool in understanding the reactivity of paramagnetic organometallic complexes that model, or serve as, intermediates in catalytic cycles. We also believe that the present study will be a paradigm for integrated experimental and theoretical studies on low oxidation state vanadium complexes and of paramagnetic organometallic complexes in general.

EXPERIMENTAL SECTION

Materials. Vanadocene (VCp_2 , bis(η^5 -2,4-cyclopentadien-1-yl)-vanadium(II)) was obtained from Strem Chemical and used without further purification. All sample manipulation was done under an inert atmosphere (Ar or N₂), and solvents were distilled and degassed before use. EPR spectroscopy showed that no V(IV) impurities were present. The importance of excluding oxygen from VCp_2 solutions for use in EPR spectroscopy cannot be overemphasized. This point was made by McConnell et al., who noted that benzene solutions of VCp_2 in air oxidized in seconds to yield EPR-active VOCP_2 ($\text{V}^{\text{IV}}, 3\text{d}^1, S = 1/2$).¹¹

HFEPR Spectroscopy. HFEPR spectra were recorded using the Electron Magnetic Resonance (EMR) Facility at the National High Magnetic Field Laboratory (NHMFL, Tallahassee, FL, USA). The spectrometer employs a Virginia Diodes (Charlottesville, VA, USA) source operating at a base frequency of 12–14 GHz and multiplied by a cascade of multipliers in conjunction with a 15/17 T superconducting magnet. Detection was provided with an InSb hot-electron bolometer (QMC Ltd., Cardiff, UK). The magnetic field was modulated at 50 kHz. A Stanford Research Systems SR830 lock-in amplifier converted the modulated signal to dc voltage. Low temperature was provided by an Oxford Instruments (Oxford, UK) continuous flow cryostat with temperature controller. Well-ground solid powder samples of VCp_2 produced very broad spectra not suitable for interpretation. Samples of VCp_2 in toluene solution (~0.1–1 M), however, gave ideal powder pattern spectra characteristic for a quartet ($S = 3/2$) spin state. These spectra were analyzed by simultaneously fitting the parameters of the standard spin Hamiltonian

$$\mathbf{H} = \beta_B \mathbf{g} \cdot \hat{\mathbf{S}} + D[\hat{S}_z^2 - S(S+1)/3] + E[\hat{S}_x^2 - \hat{S}_y^2] \quad (1)$$

to the complete two-dimensional (field vs frequency) map of turning points, following the principles of tunable-frequency EPR.²⁸ The sign of zero-field splitting (zfs) was obtained by simulating single-frequency spectra using software (program SPIN) available from A. Ozarowski.

X-Band EPR and Simulations. X-band (~9–9.5 GHz) EPR spectra were recorded on a modified Varian E-9 spectrometer using DPPH as an external standard. Spectra were simulated using the $S = 3/2$ spin Hamiltonian including ⁵¹V ($I = 7/2$, 99.75%) hyperfine coupling and nuclear Zeeman terms. The nuclear quadrupole interaction was not included, as the spectra were adequately reproduced without it. The nuclear quadrupole coupling in vanadyl complexes, as revealed by pulsed ENDOR spectroscopy, has been shown to be much smaller (~1000×) than the hyperfine coupling.²⁹ The software used (program DDPOWH) is available from J. Telser.

MCD Spectroscopy. Variable-temperature magnetic circular dichroism (MCD) spectra were collected using a spectropolarimeter (Jasco J-815) interfaced with a magneto-optical cryostat (Oxford Instruments SM 4000-8). Data were collected for solid samples of VCp_2 prepared as mulls in Fluorolube. All mull samples were generated under an argon atmosphere in a glovebox.

Computational Methods. All calculations were performed using the program package ORCA 2.8 and 2.9.³⁰ Geometry optimizations of staggered and eclipsed models of VCp_2 were performed under C_{2h} and C_{2v} symmetry constraints, using the BP86 functional^{31,32} with TZVP basis sets for all atoms.³³ (While these conformations have actual D_{5d} and D_{5h} symmetry, symmetry implementation in the program ORCA is limited to Abelian subgroups.) The resolution of identity (RI) approximation, which required the use of the TZV/J auxiliary basis set, was used in the geometry optimizations.³⁴ Ground-state zero-field splitting parameters and excited-state energies were calculated using the SORCI procedure.^{24,35} An active space of quasi-restricted V 3d orbitals (CAS 3,5) was obtained from an initial DFT calculation using the functional and basis sets described above, with the exception that the TZVP/C auxiliary basis set was employed. For the SORCI calculations, 10 quartet and 15 doublet roots were calculated, and CI thresholds were $T_{\text{sel}} = 10^{-6}$ hartrees, $T_{\text{pre}} = 10^{-4}$ hartrees, and $T_{\text{nat}} = 10^{-5}$ hartrees. Both spin–spin and spin–orbit contributions to the D -tensor (D^{SSC} and D^{SOC} , respectively) were calculated. Neither an increase in the size of the active space nor the inclusion of a greater number of roots had a significant impact on the calculated D -tensor. Ground- and excited-state properties of VCp_2 were also computed using coupled perturbed (CP)³⁶ and time-dependent (TD)^{37–40} DFT methods, respectively. These calculations utilized the B3LYP hybrid functional^{41–43} and TZVP and TZV/J basis sets in conjunction with the RIJCOSX approximation.⁴⁴ Isosurface plots of Kohn–Sham orbitals and AANOs were generated using gOpenMol⁴⁵ with isodensity values of 0.05 b^{-3} .

RESULTS AND DISCUSSION

X-Band EPR Spectroscopy of VCp_2 . The X-band EPR spectrum of VCp_2 in toluene frozen solution is virtually identical to that reported by Prins et al.^{3,12} The spectrum is characteristic for a spin quartet with $D \gg h\nu$ and axial symmetry ($S' = 1/2$, with $g'_{\perp} = 4$, $g'_{\parallel} = 2$). Spectra recorded of the parallel and perpendicular regions allowed accurate measurement of ^{51}V hyperfine splitting, $A_{\perp} = 62(2)$ MHz and $A_{\parallel} = 108(2)$ MHz, in agreement with previous reports,^{3,12} and are presented in Figure 1.

HFEPR Spectroscopy of VCp_2 . A solid sample of vanadocene produced a strong but very broad ($\Delta B_{\text{pp}} \approx 1.6$ T) resonance with $g \approx 2.40$ –2.45 at 10 K. Superimposed on that resonance were a few sharp spikes (Figure S1, Supporting Information) that we initially could not interpret. We therefore moved on to frozen solution studies with the sample dissolved in toluene (0.1–1 M). These produced very high-quality powder-pattern spectra that could be interpreted as originating from the quartet ($S = 3/2$) spin state. Figure 2 shows one of such spectra, recorded at 203.2 GHz and 10 K. Spectra obtained at other frequencies were of similarly high quality, as observed in Figures S2 and S3 (Supporting Information). The spectral quality is related to the quality of the low-temperature glass and can be best appreciated by the appearance of fairly well-resolved hyperfine structure due to the $I = 7/2$ nuclear spin of the ^{51}V nuclei (99.75% abundant), which rarely if ever appears in HFEPR spectra of magnetically nondiluted samples^{46,47} and is typically best observed at much lower frequencies such as X-band, as we show here. The hyperfine coupling (hfc) observed at 203.2 GHz is 3.84 mT, which is equivalent to 108 MHz, the same as determined for A_{\parallel} using X-band EPR. The HFEPR transition that provides this hfc is $|M_S\rangle = |+3/2\rangle \leftrightarrow |-1/2\rangle$ with z orientation, hence the correspondence with A_{\parallel} (z). It should also be noted that transitions at higher fields tend to be slightly broader because of g -strain (i.e., a distribution in g values, which effectively increases with higher field) and conceivably because of higher

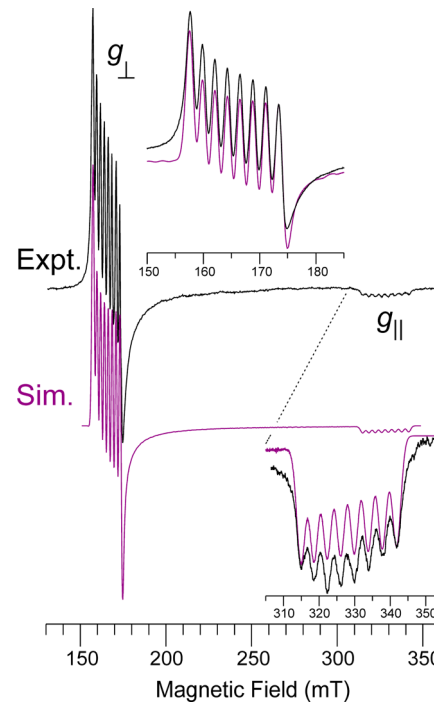


Figure 1. X-band EPR spectrum of VCp_2 in toluene frozen solution (black traces) with simulation (violet traces). The upper inset shows a detail of the perpendicular (g_{\perp}) region, and the lower inset shows a detail of the parallel (g_{\parallel}) region. Experimental conditions: ~ 0.1 mol/L, 9.24 GHz, 77 K, 0.2 mT modulation amplitude, 30 ms time constant, 8 min scan (regional scan times were 4 min, 300 ms time constant). The simulation uses $S = 3/2$, $D = 2.836$ cm $^{-1}$ (from HFEPR), $\mathbf{g} = [1.991, 1.991, 2.010]$, $\mathbf{A}^{(51)\text{V}} = [62, 62, 108]$ MHz.

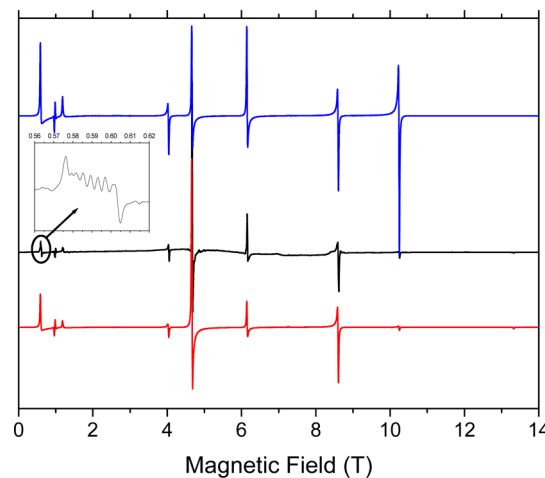


Figure 2. Main plot: HFEPR spectrum of vanadocene in toluene frozen solution, recorded at 203.2 GHz and 10 K (black trace). The colored traces are simulations obtained using spin Hamiltonian parameters as in Table 2. The blue trace uses a negative value for D ; the red trace, a positive value. Single-crystal line width used in the simulations was isotropic 10 mT, 50% Gaussian shape. Inset: Parallel turning point at ca. 0.6 T in increased resolution showing a resolved ^{51}V hyperfine structure.

order Zeeman effects as well.⁴⁸ Thus, both in this case and in a previous case (involving hfc from a ligand, $^{79,81}\text{Br}$, rather than from the metal ion),⁴⁹ hfc was resolved only at the lowest field transition. We thus suggest that in frozen solution HFEPR

studies of systems potentially with hfc of interest that efforts be made to maximize resolution only at the lowest field signal(s).

Table 1. Structural Parameters for VCp_2 Determined by X-ray Diffraction (XRD) Experiments and DFT Geometry Optimizations

	VCp_2 XRD (108 K)	VCp_2 XRD (295 K)	VCp_2 DFT (C_{2h})	VCp_2 DFT (C_{2v})
V-C ₁	2.273(1)	2.275(5)	2.289	2.289
V-C ₂	2.268(1)	2.273(5)	2.290	2.289
V-C ₃	2.260(1)	2.282(5)	2.290	2.289
V-C ₄	2.267(1)	2.257(5)	2.290	2.289
V-C ₅	2.278(1)	2.241(4)	2.290	2.289
C-C ^a	1.417	1.420	1.427	1.427
C-H ^a	0.95	ND ^b	1.091	1.091

^aAverage bond lengths are included. ^bNot determined.

Table 2. Ground-State Spin Hamiltonian Parameters for VCp_2 Determined from EPR Experiments^a and DFT Computations Using XRD- and DFT-Derived Structures

	VCp_2 experiment	VCp_2 XRD (108 K)	VCp_2 XRD (295 K)	VCp_2 DFT (C_{2h})	VCp_2 DFT (C_{2v})
g_{\perp}	1.991(2)	1.993	1.993	1.992	1.992
g_{\parallel}	2.001(2)	2.001	2.001	2.001	2.001
D (cm ⁻¹)	+2.836(2)	2.96	2.85	2.89	2.88
E (cm ⁻¹)	0.00	0.10	0.09	0.09	0.09
D^{SOC} (cm ⁻¹)	1.15	1.15	1.16	1.16	
$\alpha \rightarrow \alpha$	0.69	0.69	0.72	0.73	
$\beta \rightarrow \beta$	0.38	0.38	0.38	0.39	
$\alpha \rightarrow \beta$	0.22	0.22	0.21	0.19	
$\beta \rightarrow \alpha$	-0.14	-0.14	-0.14	-0.15	
D^{SSC} (cm ⁻¹)	1.81	1.70	1.73	1.72	
A_{\perp} (MHz)	62(2)	-56.4	-62.4	-66.2	-66.1
A_{\parallel} (MHz)	108(2)	-117.8	-123.4	-128.5	-128.2
A_{iso}	77	-76.9	-82.7	-90.0	-86.8

^aThe electronic spin Hamiltonian parameters (g and D, E) values are from HFEPR and the ^{51}V nuclear parameters ($|A_{\perp}|, |A_{\parallel}|$) from X-band EPR (all from this work), and corroborated by HFEPR. The previous, low-frequency (X- and Q-band) EPR study by Prins and van Voorst gave $g_{\perp} = 1.990(2)$, $g_{\parallel} = 2.002(1)$, $|D| = 2.7(1)$ cm⁻¹, $|A_{\perp}| = 64.4$ MHz ($21.5(5) \times 10^{-4}$ cm⁻¹), $|A_{\parallel}| = 110$ MHz ($36.7(1.0) \times 10^{-4}$ cm⁻¹); $A_{\text{iso}} = (2A_{\perp} + A_{\parallel})/3 = 79.6$ MHz.³ Their original low-frequency EPR study gave $g_{\perp} = 1.99$, $g_{\parallel} = 2.002(1)$, $|D| = 2.3$ cm⁻¹, with the same hfc.¹²

Although the agreement between simulations and experiment is close to perfect, the actual spin Hamiltonian parameters were obtained from a two-dimensional map of resonances, as shown in Figure 3. The map immediately confirms that there is a single zero-field energy gap between the two Kramers doublets in the $S = 3/2$ spin state ($M_S = \pm 1/2$ and $\pm 3/2$), and this gap amounts to approximately 166 GHz, which is equal to 5.6 cm⁻¹. For an axial zfs tensor, as is the case in vanadocene, this corresponds to $|D| = 2.8$ cm⁻¹. This value was subsequently refined by computer fits to 2.836 cm⁻¹, and the g values were found to be 2.001 and 1.991 for g_{\parallel} and g_{\perp} , respectively.

The toluene solution spectra and their interpretation allowed us to come back to the previously uninterpretable condensed-phase spectra. The single resonance of immense line width (~ 1.6 T peak-to-peak) as shown in Figure S1 is obviously a result of strong spin–spin interactions present in solid

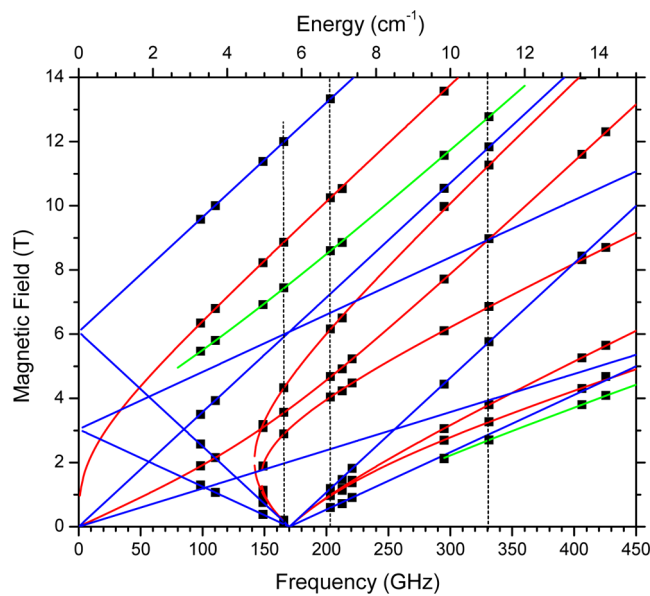


Figure 3. Two-dimensional (field vs frequency/energy) map of turning points observed in the EPR spectra of vanadocene in toluene solution at 10 K. The squares are experimental points; the lines were calculated using the best-fit spin Hamiltonian parameters as in Table 2. Blue lines: parallel; red lines: perpendicular; green lines: off-axis turning points. The vertical dashed lines represent the frequencies and field range at which spectra shown in Figure 2 (203 GHz) and Supporting Information Figures S2 (166 GHz) and S3 (331 GHz) were recorded.

vanadocene, which effectively average the zfs. The same broad resonance can also be observed at a much reduced intensity in the solution spectra, particularly at high frequencies (Figure S3) and can be explained by an undissolved residue present in the sample.⁵⁰ The sharp features in the solid, on the other hand, correspond exactly to the turning points we observed in the solution and must therefore be attributed to isolated, noninteracting vanadocene molecules. The nature of those noninteracting sites is unclear at this point but is outside the scope of the present work.

Before we proceed with the detailed analysis of spin Hamiltonian parameters obtained by HFEPR we should comment on the results of the early (1960s) EPR work on vanadocene by Prins et al.^{3,12} Having only two low frequencies at their disposal (X- and Q-band), these authors succeeded in measuring the zfs fairly well ($|D| = 2.3^{12}$ or 2.7^3 cm⁻¹ vs our value of 2.836 cm⁻¹) and g values quite accurately ($g_{\parallel} = 2.002$, $g_{\perp} = 1.99$ vs our values of 2.001 and 1.991, respectively), at the same time disproving an earlier report from the group of McConnell, who reported $D = 0.83$ cm⁻¹ ($\Delta = 2|D| = 50(3)$ GHz) for VCp_2 doped into FeCp_2 host, based on single-crystal studies at 22.5 GHz (0.75 cm⁻¹).⁵¹ Given that Prins and van Voorst also studied VCp_2 doped into FeCp_2 (albeit as a powder) and found that “within the uncertainty of the measurement the results obtained in MTHF [2-methyltetrahydrofuran], MCH [methylcyclohexane], and FeCp_2 are the same”,³ the discrepancy cannot be attributed to a chemical difference between inert solvent and FeCp_2 host. The error must be due to the difficulty of determining zfs, even from single crystals, in cases where $\Delta > \hbar\nu$, making the accurate (although perhaps not so precise) results of Prins et al.^{3,12} all the more impressive, yet also pointing out the advantage of the current availability of HFEPR.

Electronic Absorption and MCD Spectroscopy of VCp_2 . The 193 K electronic absorption spectrum of VCp_2 in toluene shows three major features from 9000 to 28 000 cm^{-1} (Figure 4, top). The onset of more intense features in the near-

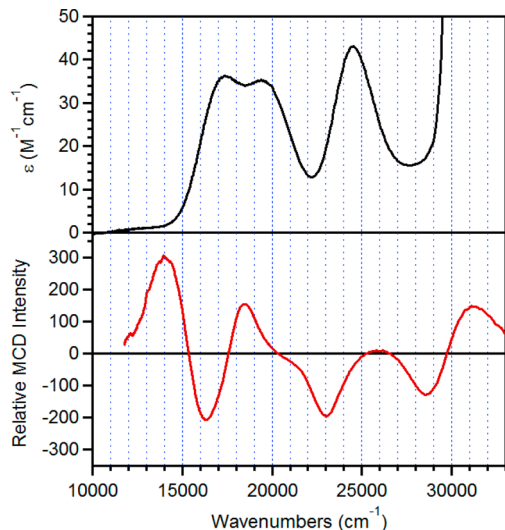


Figure 4. Top: 193 K electronic absorption spectrum of VCp_2 in toluene. Bottom: 2 K, 7 T MCD spectrum of a Fluorolube mull sample of VCp_2 .

UV region is marked by the steep rise in absorption at $\sim 29\ 000\ \text{cm}^{-1}$. This spectrum is qualitatively similar to those previously reported,^{3,52,53} although the absorption spectrum collected here shows greater resolution for the lowest energy feature than for those previously reported. It is possible that in earlier studies there was light scattering from the frozen solution.^{3,52} The variation among experimental conditions and band positions is summarized in Table S3 (Supporting Information). In our absorption spectrum, there are three bands of comparable intensity ($\epsilon \approx 35\text{--}40\ \text{M}^{-1}\ \text{cm}^{-1}$) in the visible region that are well modeled with three Gaussian bands centered at 17 000, 19 860, and 24 580 cm^{-1} (Supporting Information, Figure S4 and Table S1).⁵⁴ These three bands were previously assigned as spin-allowed $^4\text{A}_{2g} \rightarrow ^4\text{E}_{1g}$ (I), $^4\text{A}_{2g} \rightarrow ^4\text{E}_{2g}$, and $^4\text{A}_{2g} \rightarrow ^4\text{E}_{1g}$ (II) transitions, respectively, using symmetry labels from the D_{5d} point group.^{3,52} The $^4\text{E}_{1g}$ (I) and $^4\text{E}_{1g}$ (II) excited states are from the ^4F and ^4P d^3 free-ion terms, respectively. The $^4\text{A}_{2g}$ ground state of VCp_2 arises from the $(\text{a}_{1g})^1(\text{e}_{2g})^2(\text{e}_{1g})_0^0$ configuration, and the ^4E excited states arise from one-electron excitations. Specifically, the $^4\text{A}_{2g} \rightarrow ^4\text{E}_{1g}$ (I) transition corresponds to a one-electron excitation to give the $(\text{a}_{1g})^0(\text{e}_{2g})^2(\text{e}_{1g})^1$ configuration. The $^4\text{A}_{2g} \rightarrow ^4\text{E}_{2g}$ and $^4\text{A}_{2g} \rightarrow ^4\text{E}_{1g}$ (II) transitions each correspond to generation of the $(\text{a}_{1g})^1(\text{e}_{2g})^1(\text{e}_{1g})^1$ excited-state configuration.

The 2 K, 7 T MCD spectrum of VCp_2 shows a series of seven features from 11 000 to 33 000 cm^{-1} that alternate in sign (Figure 4, bottom). With the exception of the negatively signed band at 28 600 cm^{-1} , all MCD features show an increase in intensity at lower temperatures. This is referred to as C-term behavior, and it is commonly observed for complexes with paramagnetic ground states (Supporting Information, Figure S5).⁵⁵⁻⁵⁷ For VCp_2 , the MCD C-terms arise from the spin-degenerate $^4\text{A}_{2g}$ ground state and show temperature dependences reflective of the thermal population of the ground-state spin manifold split in the magnetic field. The temperature-

independent band at 28 600 cm^{-1} does increase in intensity with increasing magnetic field strength, leading to its assignment as a B-term that gains intensity through field-induced mixing of states. All paramagnetic complexes display MCD C-terms, although the larger spin-orbit coupling constants of transition metals render metal-based d-d transitions quite intense in low-temperature MCD experiments. In contrast, MCD A-terms, which are temperature-independent, arise from transitions involving orbitally degenerate ground or excited states.⁵⁵⁻⁵⁷ An A-term appears as a derivative-shaped signal whose center corresponds to the electronic transition energy. The $^4\text{A}_{2g} \rightarrow ^4\text{E}$ transitions of VCp_2 give rise to both C- and A-terms, but the C-terms dominate the low-temperature MCD spectrum.

The $^4\text{A}_{2g} \rightarrow ^4\text{E}_{1g}$ (I), $^4\text{A}_{2g} \rightarrow ^4\text{E}_{2g}$, and $^4\text{A}_{2g} \rightarrow ^4\text{E}_{1g}$ (II) transitions of VCp_2 are each expected to give rise to a pseudo-A-term in the MCD spectrum. Pseudo-A-terms, which appear as temperature-dependent, derivative-shaped signals, are observed for transitions to orbitally degenerate excited states or near-degenerate excited states that mix by spin-orbit coupling.⁵⁵ In the case of the orbitally degenerate ^4E states of VCp_2 , the excited state splitting due to in-state spin-orbit coupling is not resolved in the electronic absorption spectrum because this splitting is roughly an order of magnitude smaller than the bandwidth of the electronic transition (see discussion in the Supporting Information). However, in the MCD spectrum, transitions to the spin-orbit-split components of a ^4E state are oppositely signed, giving rise to the derivative-shaped appearance. Spin-orbit coupling splits each ^4E state into four components, which would lead to a maximum of four MCD transitions. However, at 2 K and 7 T, only the $M_S = -3/2$ component of the $^4\text{A}_{2g}$ ground state is thermally populated, which limits the observed transitions to the corresponding $M_S = -3/2$ components of the excited states (i.e., only $|^4\text{A}_{2g}, 0, -3/2\rangle \rightarrow |^4\text{E}_g, +1, -3/2\rangle$ and $|^4\text{A}_{2g}, 0, -3/2\rangle \rightarrow |^4\text{E}_g, -1, -3/2\rangle$ excitations are observed, using $|^{2S+1}\Gamma, M_L, M_S\rangle$ notation to describe the terms).

In light of these considerations, the zero-crossing point of the pseudo-A-term should roughly correspond to the energy of the electronic transition observed in the absorption spectrum. For VCp_2 , pseudo-A-terms are anticipated at 17 000, 19 860, and 24 580 cm^{-1} , with some shifting expected due to the differences in temperature and media of the absorption and MCD samples (193 K and toluene solution versus 2 K mull samples, respectively). Under the assumption that the MCD band at $\sim 14\ 000\ \text{cm}^{-1}$ is the positive component of a pseudo-A-term, the MCD spectrum of VCp_2 exhibits pseudo-A-terms at 15 400 and 20 300 cm^{-1} , in reasonable agreement with the positions of the first two absorption bands. The pseudo-A-term expected near 24 600 cm^{-1} is potentially obscured by the negative B-term at 28 600 cm^{-1} . A Gaussian deconvolution of the 2 K, 7 T MCD spectrum of VCp_2 shows the resolution of these signals in terms of eight electronic transitions (Supporting Information, Figure S6 and Table S2), although we note this deconvolution is not a unique solution. Taken together, the MCD data serve to confirm the previous assignments, which allows for the evaluation of computational predictions of excited-state energies for VCp_2 using DFT and *ab initio* methods.

DFT Computations for VCp_2 . Molecular Structures. Calculated zfs parameters can be very sensitive to minor changes in the ligand geometry around the metal center. We therefore considered several structural models in our

calculations for VCp_2 . Arguably the most relevant crystal structure is that refined using X-ray diffraction data collected at 108 K,⁵⁸ as this is the temperature most similar to that of the EPR experiments. In this structure, the Cp rings are found in a staggered orientation. Metric parameters are shown in Table 1. For comparison, we also included a structure of VCp_2 solved using XRD data collected at 295 K,⁵⁹ which shows more variation in V–C bond lengths (Table 1). A previous computational study of VCp_2 using the B3LYP functional in concert with a DZP basis set afforded a model with V–C distances of 2.312 Å,²² notably longer than the distances obtained by either XRD study. We performed DFT geometry optimizations using the BP86 functional with a TZVP basis set to obtain models of VCp_2 in the staggered (D_{5h}) and eclipsed (D_{5h}) conformations. Because ORCA supports only Abelian subgroups,³⁰ these models were optimized under the lower C_{2h} and C_{2v} symmetry constraints, respectively. In the staggered model, this lower symmetry results in one slightly shorter V–C₁ distance of 2.289 Å, relative to the other V–C distances of 2.290 Å (Table 1). In the eclipsed model, all V–C distances are equal (2.289 Å). These two conformations are essentially isoenergetic at the DFT level ($\Delta E_{\text{SCF}} = 0.08 \text{ kJ/mol}$). The calculated V–C and C–C bond lengths are slightly longer than those obtained from XRD studies. However, they are quite similar to those obtained from gas phase electron diffraction studies (V–C of 2.280(5) and C–C of 1.434 Å⁶⁰), suggesting that crystal packing and/or solvation effects can partially account for the minor discrepancy between computed and crystallographic metric parameters.

Density Functional Theory Calculations. Although it is well accepted that the $^4\text{A}_{1g}$ ground state of VCp_2 arises from three parallel spin electrons in the a_{1g} and e_{2g} orbitals (see Scheme 1), theoretical studies have provided conflicting results concerning the relative energies of these orbitals. On the basis of agreement between experimental and calculated spin Hamiltonian parameters, Prins and van Voorst determined a level ordering of $e_{2g} < a_{1g} < e_{1g}$.³ In contrast, recent DFT calculations at the B3LYP/DZP level give the a_{1g} orbital at lower energy than the e_{2g} set.²² Our spin-unrestricted BP86/TZVP calculations on both the staggered and eclipsed models of VCp_2 are in agreement with the previous DFT calculations, with the filled a_{1g} spin-up orbital 0.35 eV lower than the spin-up e_{2g} set (Figure 5 and Supporting Information Table S4). This ordering is reversed in the unoccupied spin-down MOs. The orbital ordering is conserved if the models derived from the X-ray coordinates are used. Overall, the energy gap between the a_{1g} and e_{2g} MOs varies slightly for different functionals (ranging from a maximum of 0.40 eV for the TPSSh hybrid functional to a minimum of 0.10 eV for the PBE pure functional) but is hardly affected by the size of the basis set or the inclusion of solvation effects using a continuum dielectric (see Supporting Information Table S5).

Ground-state spin Hamiltonian parameters obtained from DFT calculations for all models are in good agreement with the experimental values (Table 2). In particular, the computed g_{\perp} and g_{\parallel} values are identical to their experimental counterparts, considering the experimental uncertainty. The predicted D parameters range from 2.96 to 2.85 cm⁻¹, very close to the experimental value of 2.836(2) cm⁻¹. This high level of agreement is somewhat surprising given the known limitations, and well-documented failures,^{18–21} of DFT methods for predicting accurate zero-field splitting parameters. Because of the lower symmetry of the models, a nonzero, but quite small, E

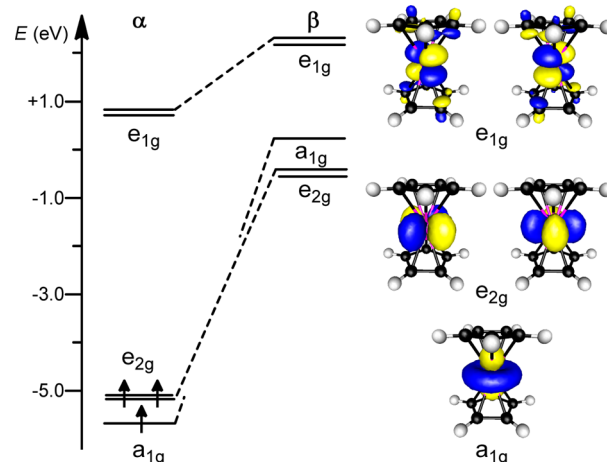


Figure 5. Relative energies of the DFT-computed Kohn–Sham orbitals (left) and isosurface plots of corresponding quasi-restricted orbitals for C_{2h} VCp_2 .

value of 0.10–0.09 cm⁻¹ is predicted for the models. The small range of calculated D and E for these species speaks to the structural similarities among the models considered. The largest variations among these four models are observed in the computed hyperfine parameters A_{\perp} and A_{\parallel} ($A_{\perp} = -56.4$ to -66.2 MHz and $A_{\parallel} = -117.8$ to -128.5 MHz). Thus, for this system, the hyperfine parameters appear to be more sensitive to minor structural changes than the zero-field splitting parameters. In all cases, however, the computed hyperfine values are close in magnitude to their experimental counterparts ($|A_{\perp}| = 62(2) \text{ MHz}$ and $|A_{\parallel}| = 108(2) \text{ MHz}$), particularly using the 108 K XRD structure. The other three models give hyperfine parameters slightly too large in magnitude, which could be due to too much 4s character in the a_{1g} MO in these cases. The negative signs of A_{\perp} and A_{\parallel} were anticipated previously using ligand-field theory expressions for these parameters that considered the metal–ligand covalency of the e_{2g} and a_{1g} orbitals.³ Reasonable metal–ligand covalencies were obtained only when A_{\perp} and A_{\parallel} were of the same sign, and the corresponding D values were used to argue in favor of both parameters being negatively signed.

The DFT calculations offer a means of comparing the spin–orbit coupling (D^{SOC}) and electron–electron spin–spin coupling (D^{SSC}) contributions to D (Table 2). Previous calculations had found that these terms contribute almost equally to D ($D^{\text{SOC}} = 1.4 \text{ cm}^{-1}$ and $D^{\text{SSC}} = 1.9 \text{ cm}^{-1}$), although it should be noted that in that early study the aim was to obtain an order of magnitude estimate for D^{SSC} to understand the general importance of this term,³ which is often neglected in consideration of zfs in transition metal complexes.⁶¹ The DFT calculations give values for D^{SOC} and D^{SSC} (1.15 and 1.81–1.70 cm⁻¹, respectively) that are remarkably similar to the previously calculated values. Given that ligand contributions to D^{SSC} were intentionally neglected in the early study, their method of treating this term using the dipolar spin–spin operator and a basis set of 3d Slater orbitals worked exceptionally well. The contributions to D^{SOC} from the DFT calculations can be further broken down into excitations to excited states of the same spin as the ground state ($\alpha \rightarrow \alpha$ and $\beta \rightarrow \beta$ transitions) or excited states differing in one unit of spin-angular moment relative to the ground state ($\alpha \rightarrow \beta$ and $\beta \rightarrow \alpha$ transitions). For all models of VCp_2 , contributions from spin-flip transitions ($\alpha \rightarrow \beta$ and $\beta \rightarrow \alpha$)

$\rightarrow \alpha$) are of the opposite sign and of similar magnitudes (Table 2). Consequently, the contributions from these states represent only $\sim 7\%$ of D^{SOC} . The major contribution is from the $\alpha \rightarrow \alpha$ and $\beta \rightarrow \beta$ transitions. This result is in contrast to the previous calculations, where the largest contribution to D^{SOC} was from the low-lying ${}^2A_{1g}$ excited state. Given this discrepancy, as well as the fact that DFT computations have limitations in the treatment of spin-flip transitions and orbitally degenerate states,⁶² we performed multireference SORCI computations for comparison.

Multireference SORCI Calculations. In a SORCI calculation, a multireference wave function is constructed using approximate average natural orbitals (AANOs), which facilitates a more balanced treatment of electron correlation in each state. In addition, SORCI employs a difference-dedicated configuration interaction procedure, ideally leading to more accurate energy differences between states, and thus better descriptions of properties dependent on these energy differences. This method has been shown to provide highly accurate zfs parameters^{18,21,63} and has had success even in cases where CASSCF methods have failed.¹⁹ The major drawback of the SORCI approach is the high computational demand, often necessitating the use of truncated systems. However, VCp₂, which is small in size (11 non-H atoms), contains a single heavy atom, and has only three unpaired electrons, is ideally suited for the SORCI method. Indeed, this system was easily treated without truncation using TZVP basis sets on all atoms and a CAS(3,5).

The SORCI calculations yield a ${}^4A_{1g}$ ground state, and the leading configuration in the SORCI ground-state wave function is $(e_{2g})^2(a_{1g})^1(e_{1g})^0$ (90%), where the e_{2g} AANOs are listed below the a_{1g} AANO. The AANOs are qualitatively similar to the Kohn–Sham orbitals described earlier, and isosurface plots of the former are provided in the Supporting Information (Figure S7). It should be noted, however, that, because the AANOs are constructed using the average density matrix of all states, their ordering should not be taken to be reflective of the MO energy levels.

The SORCI-computed D parameters are in remarkable agreement with the experimental value as summarized in Table 3. The largest deviation is only 0.04 cm^{-1} , which is observed for the C_{2v} model and that derived from the 108 K XRD structure. Consistent with the results of our DFT calculations, there are only minor differences in D and E among the four models. The most dramatic differences between the DFT- and SORCI-computed D values are the contributions from the D^{SOC} and D^{SSC} terms. Whereas the DFT calculations predict a slightly

larger contribution from D^{SSC} (Table 2), the SORCI calculations predict the D^{SOC} to be dominant ($D^{\text{SOC}} = 2.3$ and $D^{\text{SSC}} = 0.6 \text{ cm}^{-1}$; see Table 3). Thus, under the very reasonable expectation that the SORCI computations provide more accurate treatment of zfs, the DFT computations predict an appropriate value for D only through the cancellation of error, as the D^{SOC} and D^{SSC} terms are predicted to be too large and too small, respectively, by nearly a factor of 2.

Contributions to D^{SOC} from individual excited states are also readily obtained from the SORCI computations and are listed in Table 4. Focusing specifically on the fully optimized C_{2h}

Table 4. Configurations, Energies (cm^{-1}), and SOC Contributions to D from Excited States of C_{2h} VCp₂ Obtained from SORCI Computations

state	configuration	energy	D
${}^4A_{2g}$	$(e_{2g})^2(a_{1g})^1(e_{1g})^0$	0	
${}^2E_{1g}$	$(e_{2g})^2(a_{1g})^1(e_{1g})^0$	9 706	0.00
		9 926	0.00
${}^2A_{1g}$	$(e_{2g})^2(a_{1g})^1(e_{1g})^0$	11 536	1.80
${}^4E_{1g}$ (I)	$(e_{2g})^2(a_{1g})^0(e_{1g})^1$	18 157	0.34
		18 241	0.34
${}^4E_{2g}$	$(e_{2g})^1(a_{1g})^1(e_{1g})^1$	19 842	0.00
		20 000	0.00
${}^4E_{1g}$ (II)	$(e_{2g})^1(a_{1g})^1(e_{1g})^1$	25 650	0.00
		25 806	0.00
${}^2E_{1g}$	$(e_{2g})^2(a_{1g})^0(e_{1g})^1$	28 009	0.00
		28 003	-0.03
${}^2E_{1g}$	$(e_{2g})^2(a_{1g})^0(e_{1g})^1$	28 057	0.00
		28 097	-0.02
${}^2A_{1g}$	$(e_{2g})^1(a_{1g})^1(e_{1g})^1$	29 152	-0.19

VCp₂, the largest contribution to D^{SOC} comes from the ${}^2A_{1g}$ excited state ($D = 1.80 \text{ cm}^{-1}$) that derives from the same $(e_{2g})^2(a_{1g})^1(e_{1g})^0$ configuration as the ${}^4A_{1g}$ ground state. Thus, one reason why the DFT calculations so greatly underestimate D^{SOC} is because of the poor treatment in DFT of excited states of a different multiplicity than the ground state. The only other major contribution to D^{SOC} comes from the lowest lying ${}^4E_{1g}$ excited state ($D = 0.68 \text{ cm}^{-1}$). A small negative contribution to D^{SOC} arises from the higher energy ${}^2A_{1g}$ state that derives from the $(e_{2g})^1(a_{1g})^1(e_{1g})^1$ configuration. These results are in good agreement with previous ligand-field calculations that determined the ${}^4E_{1g}$, ${}^2A_{1g}$, and ${}^2E_{1g}$ states to respectively contribute 0.34, 1.36, and -0.22 cm^{-1} to D^{SOC} .³ The main differences are that the SORCI calculations predict contributions from a second, higher-energy ${}^2A_{1g}$ state instead of ${}^2E_{1g}$ states, which contribute negligibly to D^{SOC} .

Comparison of Excited-State Energies from Ligand-Field Theory (LFT), SORCI, and TD-DFT Computations. Prins and van Voorst used LFT to analyze their absorption spectra and thereby extract energies of the ${}^4E_{1g}$ (I), ${}^4E_{2g}$, and ${}^4E_{1g}$ (II) excited states, which then gave energies of the e_{2g} , a_{1g} , and e_{1g} orbitals.³ In parallel with our quantum chemical calculations, we wished to confirm these original results using LFT in which an exact calculation is performed (matrix diagonalization of the entire d^3 basis set). This process is described in detail in the Supporting Information. The conclusion is that Prins and van Voorst's model, in which the e_{2g} orbitals are below a_{1g} in energy, is fully validated with only a slight refinement of the energy levels of these orbitals (see Table S6, Supporting Information).

Table 3. Zero-Field Splitting Parameters (in cm^{-1}) Calculated for Models of VCp₂ Using SORCI Computations with XRD- and DFT-Derived Structures^a

	VCp ₂ XRD (108 K)	VCp ₂ XRD (295 K)	VCp ₂ DFT (C_{2h})	VCp ₂ DFT (C_{2v})
D	2.90	2.86	2.87	2.90
E	0.18	0.16	0.16	0.19
D^{SOC}	2.25	2.22	2.27	2.26
D^{SSC}	0.65	0.64	0.60	0.64

^aExperimental values for all spin Hamiltonian parameters are given in Table 2; for ease of comparison we repeat here: $D = +2.836(2)$; LFT calculations (see Supporting Information) give $D^{\text{SOC}} = 1.4$; Prins and van Voorst also calculated spin–spin coupling by several methods and obtained $D^{\text{SSC}} = 0.2–1.9$, depending on the orbital type used.³

Table 5. Ligand-Field States, Configurations (Using D_{5d} Symmetry Labels), and Energies (cm^{-1}) Calculated for the DFT-Energy-Minimized Model of Staggered VCp_2 (C_{2h}) Using TD-DFT and SORCI Methods

state	configuration	excitation	exptl (Abs)	SORCI	TD-DFT
$^4\text{A}_{2g}$	$(\text{e}_{2g})^2(\text{a}_{1g})^1(\text{e}_{1g})^0$		0	0	0
$^4\text{E}_{1g}$ (I)	$(\text{e}_{2g})^2(\text{a}_{1g})^0(\text{e}_{1g})^1$	$\text{a}_{1g} \rightarrow \text{e}_{1g}$	17 000 ^a	18 157	19 534
				18 241	19 583
$^4\text{E}_{2g}$	$(\text{e}_{2g})^1(\text{a}_{1g})^1(\text{e}_{1g})^1$	$\text{e}_{2g} \rightarrow \text{e}_{1g}$	19 860 ^a	19 842	18 674
				20 000	18 685
$^4\text{E}_{1g}$ (II)	$(\text{e}_{2g})^1(\text{a}_{1g})^1(\text{e}_{1g})^1$	$\text{e}_{2g} \rightarrow \text{e}_{1g}$	24 580 ^a	25 650	24 375
				25 806	24 391
$^2\text{A}_{1g}$	$(\text{e}_{2g})^2(\text{a}_{1g})^1(\text{e}_{1g})^0$		10 560 ^b	11 536	
$^2\text{E}_{1g}$	$(\text{e}_{2g})^2(\text{a}_{1g})^1(\text{e}_{1g})^0$		7040 ^b	9706	
				9926	

^aThese bands were originally reported by Prins and van Voorst as appearing respectively at 17 600, 19 700, and 24 600 cm^{-1} .³ See Table S3 for a summary of literature absorption spectroscopic data on VCp_2 . ^bThe values for the $^2\text{A}_{1g}$ and $^2\text{E}_{1g}$ excited states were determined by taking the energies of these states as $4B + 5C$ and $4B + 3C$, respectively, and using $B = 440 \text{ cm}^{-1}$ and $C = 4B$.³ As described in the SI, fitting of LFT parameters gives the energies of $^2\text{A}_{1g}$ and $^2\text{E}_{1g}$ at 10 800 and 7400 cm^{-1} , respectively, which are slightly closer to the SORCI-calculated values (see Tables S8–S10).

Another LFT model was used by Pavlík et al.,⁵² which is based on treating the D_{5d} symmetry metallocene (and analogous D_{6d} bisarenes) effectively as a $C_{\infty v}$ system. This approach has been thoroughly discussed in a number of papers by Warren^{53,64–66} and will not be expounded on here. We have, however, used the LF parameters derived by Pavlík et al.,⁵² also to model successfully the electronic transitions and added SOC. This process is described in detail in the Supporting Information (see Tables S11 and S12).

The net result of this revisiting of earlier LFT analyses is that these methods are fully validated and provide a good description of the electronic transitions, in terms of both their assignment and their energy match using reasonable bonding and interelectronic repulsion (Racah) parameters. However, in all of these applications of LFT, although the sign is correct, the magnitude of D^{SOC} is consistently underestimated (roughly 50% of the SORCI-calculated and presumed experimental values). We have no explanation as to why this is the case, except to note that the calculation of such small energies is always fraught with difficulties and the LFT models are simplistic in their use of only a metal d-orbital basis set.

The SORCI calculations for the fully optimized C_{2h} model of VCp_2 yield energies for the $^4\text{E}_{1g}$ (I), $^4\text{E}_{2g}$, and $^4\text{E}_{1g}$ (II) excited states at $\sim 18\,200$, $19\,900$, and $25\,700 \text{ cm}^{-1}$, respectively, which are in full support of these band assignments (Table 5). Because of the lower symmetry of the VCp_2 model, each of the E excited states is split into two components that differ in energy by only $\sim 150 \text{ cm}^{-1}$. The largest deviation between the SORCI-computed and experimental excited-state energies is for the lowest energy $^4\text{E}_{1g}$ (I) state. This relatively small discrepancy of 1300 cm^{-1} is consistent with previous benchmark calculations using the SORCI method for open-shell transition metal complexes, supporting the relatively high accuracy of this approach.³⁵

For comparison, we also calculated excited-state energies for C_{2h} VCp_2 using the more commonly employed TD-DFT method (Table 5). Consistent with the experimental results, the TD-DFT computations predict three ligand-field transitions in the range $18\,500$ – $25\,000 \text{ cm}^{-1}$. However, contrary to the band assignments and the results of the SORCI computations, the TD-DFT method predicts $^4\text{E}_{2g}$ as the lowest energy quartet excited state ($18\,700 \text{ cm}^{-1}$), with the $^4\text{E}_{1g}$ (I) excited state lying

at slightly higher energy ($19\,500 \text{ cm}^{-1}$). This error in excited-state ordering likely comes from two factors. First, in the DFT calculations the spin-up a_{1g} MO lies at lower energy than the e_{2g} orbital. This will cause the $^4\text{E}_{1g}$ (I) state, which involves a one-electron $\text{a}_{1g} \rightarrow \text{e}_{1g}$ excitation, to lie at too high an energy relative to the $^4\text{E}_{2g}$ and $^4\text{E}_{1g}$ states that arise from an $\text{e}_{2g} \rightarrow \text{e}_{1g}$ one-electron excitation. Of potentially more importance, the TD-DFT calculations do not account for configuration interaction between the $^4\text{E}_{1g}$ (I) and $^4\text{E}_{1g}$ (II) excited states. This mixing shifts the $^4\text{E}_{1g}$ (I) and $^4\text{E}_{1g}$ (II) states to lower and higher energy, respectively. In the SORCI calculations, configuration interaction between excited states is properly treated. It is noteworthy, however, that the absolute errors in energies in the TD-DFT calculations are minor ($\sim 2000 \text{ cm}^{-1}$) and well within the expected accuracy of this method. Indeed, because the TD-DFT-predicted band pattern is in good agreement with the experimental electronic absorption spectrum, if the TD-DFT calculations for C_{2h} VCp_2 were taken alone without further analysis, then the experimental bands at $17\,600$ and $19\,700 \text{ cm}^{-1}$ would be erroneously assigned as the $^4\text{A}_{2g} \rightarrow ^4\text{E}_{2g}$ and $^4\text{A}_{2g} \rightarrow ^4\text{E}_{1g}$ (I) transitions, respectively.

Lastly, we can return to the simple MO diagram in Scheme 1. We note that a vanadocene species, $[\text{V}^{\text{III}}\text{Cp}_2]^+$, would have a ground-state configuration that is either $(\text{e}_{2g})^2(\text{a}_{1g})^0(\text{e}_{1g})^0$ (giving a $^3\text{A}_{2g}$ ground state that would be suitable for HFEPR) or diamagnetic $(\text{a}_{1g})^2(\text{e}_{2g})^0(\text{e}_{1g})^0$ ($^1\text{A}_{1g}$), so that vanadocene could shed light on its neutral congener, as well as be of inherent interest. Unfortunately, such Cp species appear to be too reactive for study, and only decamethylcyclopentadienyl (Cp^*) complexes have been reported,^{67,68} $[\text{VCp}^*]^+$, in which the Cp^* methyl group binds to the V^{III} , yielding a complex radically different structurally and electronically from those of interest here. Moving to the adjacent element, CrCp_2 is notable in that it is proposed to have a_{1g} lower in energy than e_{2g} ,⁸ which is what DFT predicted for vanadocene. We plan to investigate chromocene both experimentally and computationally, including the species isoelectronic with vanadocene, chromocenium, $[\text{Cr}^{\text{III}}\text{Cp}_2]^+$, which was reported fifty years ago as a stable complex.⁶⁹

CONCLUSIONS

Taken together, this work both illustrates the high quality of the EPR and ligand-field analyses that had previously been performed on VCp_2 nearly fifty years ago and refines the current understanding of the magnetic and electronic properties of this legendary organometallic complex. The HFEPR experiments on VCp_2 establish a precise value for the axial zfs parameter D ($2.836(2) \text{ cm}^{-1}$) and confirm the absence of rhombic zfs (E), indicating that in solution, where distortions imposed by crystal packing are absent, the complex indeed has (overall) 5-fold symmetry. A general conclusion is the applicability of HFEPR toward the understanding of paramagnetic organometallic complexes, which we have shown elsewhere for V^{II} .²⁷ What is also of interest here is that resolved hfc was observed (for ^{51}V) in HFEPR spectra. Hyperfine coupling directly gives valuable information on covalency and spin distribution, and thus its determination has been one of the major contributions of conventional EPR to inorganic and organometallic chemistry. Indeed, in the case of VCp_2 , the hfc was easily determined by X-band EPR, but when complexes are “silent” to conventional EPR and have suitable magnetic nuclei (e.g., ^{55}Mn and ^{59}Co , as well as ^{51}V), only by HFEPR could one in principle obtain this information. Our previous experience of HFEPR studies on $S > 1/2$ systems having significant zfs has been disappointing with regard to observing hfc. Yet as shown here, it is possible to obtain hfc from a frozen solution HFEPR spectrum, but one needs to focus on the lowest field signal(s) to mitigate field-dependent broadening effects. Although it was unnecessary here, we suspect that signal averaging (over the low, narrow field range of the signal of interest) combined with taking a second derivative (and other data “massaging” tools) might allow hfc to be extracted from HFEPR spectra more commonly.

Previous ligand-field band assignments were verified experimentally and computationally using low-temperature MCD spectroscopy and multireference *ab initio* methods. These results confirmed the original proposal that the e_{2g} ($d_{x^2-y^2}, d_{xy}$) MOs are lower in energy than the a_{1g} (d_z^2) MO, in contrast to a later proposal based on DFT calculations²² (and our own DFT results). This work also provides a further example of DFT methods affording misleading results. For example, CP-DFT calculations for all models of VCp_2 yield D values within 4.4% of the experimental value, which is exceptional. However, the multireference SORCI calculations, which yield D values within 2.2% of the experimental value, provide evidence that the success of the CP-DFT calculations lies in cancellation of error in the D^{SOC} and D^{SSC} terms. In particular, the D^{SOC} term computed by the CP-DFT method is underestimated by nearly a factor of 2, which is directly related to the poor treatment of spin-flip excited states. In addition, the lack of configuration interaction between TD-DFT-computed excited states leads to an erroneous ordering of ligand-field excited states. It is noteworthy that both of these errors in the DFT methods are properly accounted for in the SORCI calculations or in a “traditional” ligand-field theory analysis of VCp_2 , although the latter certainly benefits from the relatively small metal–ligand covalency in the d-based frontier orbitals.

ASSOCIATED CONTENT

Supporting Information

This material is available free of charge via the Internet at <http://pubs.acs.org>.

AUTHOR INFORMATION

Corresponding Author

*E-mail: taj@ku.edu (T.A.J.); jtelsel@roosevelt.edu (J.T.).

Notes

The authors declare no competing financial interest.

ACKNOWLEDGMENTS

This work has been supported by the NHMFL, which is funded by NSF (Cooperative Agreement DMR 0654118), the State of Florida, and DOE. T.A.J. acknowledges the American Chemical Society Petroleum Research Fund (50287-DNI3) for support. D.J.M. thanks the Chemical Sciences, Geosciences and Biosciences Division, Office of Basic Energy Science, Office of Science, U.S. Department of Energy (DE-FG02-07ER15893), for financial support.

REFERENCES

- (1) Rettig, M. F.; Drago, R. S. *J. Am. Chem. Soc.* **1969**, *91*, 3432–3441.
- (2) Ammeter, J. H.; Zoller, L.; Bachmann, J.; Baltzer, P.; Gamp, E.; Bucher, R.; Deiss, E. *Helv. Chim. Acta* **1981**, *64*, 1063–1082.
- (3) Prins, R.; van Voorst, J. D. W. *J. Chem. Phys.* **1968**, *49*, 4665–4673.
- (4) Switzer, M. E.; Wang, R.; Rettig, M. F.; Maki, A. H. *J. Am. Chem. Soc.* **1974**, *96*, 7669–7674.
- (5) Ammeter, J. H. *J. Magn. Reson.* **1978**, *30*, 299–325.
- (6) Walter, M. D.; Sofield, C. D.; Booth, C. H.; Andersen, R. A. *Organometallics* **2009**, *28*, 2005–2019.
- (7) Weber, J.; Goursot, A.; Penigault, E.; Ammeter, J. H.; Bachmann, J. *J. Am. Chem. Soc.* **1982**, *104*, 1491–1506.
- (8) König, E.; Schnakig, R.; Kanellakopulos, B.; Klenze, R. *Chem. Phys. Lett.* **1977**, *50*, 439–441.
- (9) Baltzer, P.; Furrer, A.; Hulliger, J.; Stebler, A. *Inorg. Chem.* **1988**, *27*, 1543–1548.
- (10) Abbreviations used: AANO, approximate average natural orbital; CASSCF, complete active space self-consistent field; DFT, density functional theory; EPR, electron paramagnetic resonance; hfc, hyperfine coupling; HFEPR, high-frequency and -field EPR; INS, inelastic neutron scattering; LFT, ligand-field theory; MCD, magnetic circular dichroism; SOC, spin–orbit coupling; SORCI, spectroscopically oriented configuration interaction; SSC, spin–spin coupling; XRD, X-ray diffraction; zfs, zero-field splitting.
- (11) McConnell, H. M.; Porterfield, W. W.; Robertson, R. E. *J. Chem. Phys.* **1959**, *30*, 442–443.
- (12) Prins, R.; Biloen, P.; van Voorst, J. D. W. *J. Chem. Phys.* **1967**, *46*, 1216–1217.
- (13) Prins, R. *Mol. Phys.* **1970**, *19*.
- (14) Ammeter, J. H.; Swalen, J. D. *J. Chem. Phys.* **1972**, *57*, 678–698.
- (15) Krzystek, J.; Ozarowski, A.; Telser, J. *Coord. Chem. Rev.* **2006**, *250*, 2308–2324.
- (16) Neese, F. *J. Biol. Inorg. Chem.* **2006**, *11*, 702–711.
- (17) Siegbahn, P. E. M. *J. Biol. Inorg. Chem.* **2006**, *11*, 695–701.
- (18) Liakos, D. G.; Ganyushin, D.; Neese, F. *Inorg. Chem.* **2009**, *48*, 10572–10580.
- (19) Ye, S.; Neese, F.; Ozarowski, A.; Smirnov, D.; Krzystek, J.; Telser, J.; Liao, J.-H.; Hung, C.-H.; Chu, W.-C.; Tsai, Y.-F.; Wang, R.-C.; Chen, K.-Y.; Hsu, H.-F. *Inorg. Chem.* **2010**, *49*, 977–988.
- (20) Zein, S.; Duboc, C.; Lubitz, W.; Neese, F. *Inorg. Chem.* **2008**, *47*, 134–142.
- (21) Maganas, D.; Sottini, S.; Kyritsis, P.; Groenen, E. J. J.; Neese, F. *Inorg. Chem.* **2011**, *50*, 8741–8754.
- (22) Xu, Z.-F.; Xie, Y.; Feng, W.-L.; Schaefer, H. F., III. *J. Phys. Chem. A* **2003**, *107*, 2716–2729.
- (23) Ye, S.; Neese, F. *J. Chem. Theory Comput.* **2012**, *8*, 2344–2351.
- (24) Neese, F. *J. Chem. Phys.* **2003**, *119*, 9428–9443.
- (25) Mindiola, D. J. *Acc. Chem. Res.* **2006**, *39*, 813–821.

- (26) Kilgore, U. J.; Sengelaub, C. A.; Fan, H.; Tomaszewski, J.; Karty, J. A.; Baik, M.-H.; Mindiola, D. J. *Organometallics* **2009**, *28*, 843–852.
- (27) Tran, B. L.; Singhal, M.; Park, H.; Lam, O. P.; Pink, M.; Krzystek, J.; Ozarowski, A.; Telser, J.; Meyer, K.; Mindiola, D. J. *Angew. Chem., Int. Ed.* **2010**, *49*, 9871–9875.
- (28) Krzystek, J.; Zvyagin, S. A.; Ozarowski, A.; Trofimko, S.; Telser, J. *J. Magn. Reson.* **2006**, *178*, 174–183.
- (29) Grant, C. V.; Ball, J. A.; Hamstra, B. J.; Pecoraro, V. L.; Britt, R. D. *J. Phys. Chem. B* **1998**, *102*, 8145–8150.
- (30) Neese, F. ORCA - an ab initio, Density Functional and Semiempirical Program Package, 2.9; Universität Bonn: Bonn, Germany, 2010.
- (31) Becke, A. D. *J. Chem. Phys.* **1986**, *84*, 4524–4529.
- (32) Perdew, J. P. *Phys. Rev. B* **1986**, *33*, 8822–8824.
- (33) Schäfer, A.; Horn, H.; Ahlrichs, R. *J. Chem. Phys.* **1992**, *97*, 2571–2577.
- (34) Neese, F. *J. Comput. Chem.* **2003**, *24*, 1740–1747.
- (35) Neese, F.; Petrenko, T.; Ganyushin, D.; Olbrich, G. *Coord. Chem. Rev.* **2007**, *251*, 288–327.
- (36) Neese, F. *J. Chem. Phys.* **2007**, *127*, 164112.
- (37) Hirata, S.; Head-Gordon, M. *Chem. Phys. Lett.* **1999**, *314*, 291–299.
- (38) Hirata, S.; Head-Gordon, M. *Chem. Phys. Lett.* **1999**, *302*, 375–382.
- (39) Casida, M. E.; Jamorski, C.; Casida, K. C.; Salahub, D. R. *J. Chem. Phys.* **1998**, *108*, 4439–4449.
- (40) Bauernschmitt, R.; Ahlrichs, R. *Chem. Phys. Lett.* **1996**, *256*, 454–464.
- (41) Becke, A. D. *J. Chem. Phys.* **1993**, *98*, 5648–5652.
- (42) Becke, A. D. *J. Chem. Phys.* **1993**, *98*, 1372–1377.
- (43) Lee, C.; Yang, W.; Parr, R. G. *Phys. Rev. B* **1988**, *37*, 785–789.
- (44) Neese, F.; Wennmohs, F.; Hansen, A.; Becker, U. *Chem. Phys.* **2009**, *356*, 98–109.
- (45) Laaksonen, L. *J. Mol. Graphics* **1992**, *10*, 33–34.
- (46) HFEPR of doped single crystals has revealed ^{51}V hyperfine coupling in $[\text{V}(\text{H}_2\text{O})_6]^{3+}$.
- (47) Tregenna-Piggott, P. L. W.; Weihe, H.; Bendix, J.; Barra, A.-L.; Güdel, H.-U. *Inorg. Chem.* **1999**, *38*, 5928–5929.
- (48) McGavin, D. G.; Tenant, W. C.; Weil, J. A. *J. Magn. Reson.* **1990**, *87*, 92–109.
- (49) Nieto, I.; Bontchev, R. P.; Ozarowski, A.; Smirnov, D.; Krzystek, J.; Telser, J.; Smith, J. M. *Inorg. Chim. Acta* **2009**, *362*, 4449–4460.
- (50) We began with a high concentration solution, ~ 1 M, but lowering to 0.1 M still gave an excellent S/N ratio.
- (51) Dearman, H. H.; Porterfield, W. W.; McConnell, H. M. *J. Chem. Phys.* **1961**, *34*, 696–697.
- (52) Pavlík, I.; Černý, V.; Maxová, E. *Collect. Czech. Chem. Commun.* **1972**, *37*, 171–195.
- (53) Gordon, K. R.; Warren, K. D. *Inorg. Chem.* **1978**, *17*, 987–994.
- (54) The very weak absorption intensity observed at $\sim 12\ 000$ – $14\ 000\ \text{cm}^{-1}$ was previously attributed to spin-forbidden d-d transitions that gain intensity through spin-orbit coupling with nearby spin-allowed d-d transitions. 52 As described in the Supporting Information (see, for example, Table S10), multreference ab initio computations predict $^4\text{A}_{2g} \rightarrow (^2\text{E}, ^2\text{A}_{1g}, ^2\text{A})$ d-d transitions from 11 300 to 15 200 cm^{-1} , which provides some support for this previous assignment. Under the assumption that this assignment is correct, it is possible that the positive MCD C-term centered at 14 000 cm^{-1} (Figure 4, bottom) is either a spin-forbidden d-d transition or a portion of a spin-allowed d-d band with contributions from spin-forbidden d-d transitions. Given the high MCD intensity of this feature, we favor the latter assignment. However, in the Supporting Information (see Table S11) we also explore an assignment as a purely spin-forbidden band.
- (55) Piepho, S. B.; Schatz, P. N. *Group Theory in Spectroscopy with Applications to Magnetic Circular Dichroism*; Wiley: New York, 1983; pp xxv, 634.
- (56) Neese, F.; Solomon, E. I. *Inorg. Chem.* **1999**, *38*, 1847–1865.
- (57) Kirk, M. L.; Peariso, K. *Curr. Opin. Chem. Biol.* **2003**, *7*, 220–227.
- (58) Antipin, M. Y.; Boese, R. *Acta Crystallogr.* **1996**, *B52*, 314–322.
- (59) Rogers, R. D.; Atwood, J. L.; Foust, D.; Rausch, M. D. *J. Chem. Crystallogr.* **1981**, *11*, 183–188.
- (60) Gard, E.; Haaland, A.; Novak, D. P.; Seip, R. *J. Organomet. Chem.* **1975**, *88*, 181–189.
- (61) Ganyushin, D.; Gilka, N.; Taylor, P. R.; Marian, C. M.; Neese, F. *J. Chem. Phys.* **2010**, *132*, 144111.
- (62) Neese, F. *Coord. Chem. Rev.* **2009**, *253*, 526–563.
- (63) Neese, F. *J. Am. Chem. Soc.* **2006**, *128*, 10213–10222.
- (64) Warren, K. D. *J. Phys. Chem.* **1973**, *77*, 1681–1686.
- (65) Warren, K. D. *Struct. Bonding* **1976**, *27*, 45–159.
- (66) Warren, K. D. *Inorg. Chem.* **1974**, *13*, 1317–1324.
- (67) Bouwkamp, M. W.; Budzelaar, P. H. M.; Meetsma, A.; Hessen, B. *J. Organomet. Chem.* **2011**, *696*, 1920–1924.
- (68) Bouwkamp, M. W.; Budzelaar, P. H. M.; Gercama, J.; Del Hierro Morales, I.; de Wolf, J.; Meetsma, A.; Troyanov, S. I.; Teuben, J. H.; Hessen, B. *J. Am. Chem. Soc.* **2005**, *127*, 14310–14319.
- (69) Fischer, E. O.; Ulm, K. *Chem. Ber.* **1962**, *95*, 692–694.